Applied Magnetic Resonance (2020) 51:1177–1200
https://doi.org/10.1007/s00723-020-01246-6

Applied
Magnetic Resonance

REVIEW

Influence of Hyperfine Coupling Strain on Two-Dimensional ESEEM Spectra from $I=1/2$ Nuclei

Sergei A. Dikanov[1] · **Alexander T. Taguchi**[2]

Received: 30 June 2020 / Revised: 30 July 2020 / Published online: 30 August 2020

Abstract

HYSCORE, a variant of two-dimensional ESEEM spectroscopy, is currently one of the most effective tools in high-resolution solid-state EPR spectroscopy. Our systematic studies of hydrogen bonds with semiquinones in ^{15}N-labeled proteins have previously provided us with an extensive collection of ^{15}N HYSCORE spectra produced by N–H…O nitrogen donors. Examination of these spectra has indicated in several cases lineshape distortions not described by available theoretical models. We were able to explain all observed artificial phenomena in the ^{15}N spectra of semiquinones considering a single mechanism—strain of the isotropic hyperfine interaction. In this review article, we introduce the HYSCORE experiment and the theoretical background for spectra of $I=1/2$ nuclei in orientation-disordered samples. We then present a description of the observed lineshape distortions and an explanation of the hyperfine strain's influence on the experimental spectra. In the final part of the article, we discuss (i) similar lineshape distortions found in previously published spectra from ^{15}N, ^{29}Si, ^{31}P, and ^{57}Fe nuclei that can be explained using the approach applied for the analysis of the ^{15}N spectra of semiquinones, and (ii) a recently published analysis of ^{31}P spectra with a different type of lineshape distortion based on a more sophisticated method, where the strength of anisotropic coupling is correlated with the sign and value of the isotropic constant in different conformations of a Cu(II) complex.

Electronic supplementary material The online version of this article (https://doi.org/10.1007/s00723-020-01246-6) contains supplementary material, which is available to authorized users.

Material described in this article was presented at the International Conference "Magnetic Resonance – Current State and Future Perspectives" (EPR-75) devoted to the 75th anniversary of the discovery of EPR (Kazan, September 23–27, 2019).

✉ Sergei A. Dikanov
dikanov@illinois.edu

[1] Department of Veterinary Clinical Medicine, University of Illinois at Urbana-Champaign, Urbana, IL 61801, USA

[2] RubrYc, Inc., 733 Industrial Road, San Carlos, CA 94403, USA

1 Introduction

Since its discovery in 1944 by E. K. Zavoisky of electron paramagnetic resonance (EPR), or electron spin resonance (ESR) spectroscopy [1], EPR has been heralded over the past 75 years as a very sensitive and informative technique in scientific research and practical applications for the characterization of paramagnetic species and their chemical properties. Key turning points in the history of EPR were the developments of high-resolution techniques such as continuous wave (CW), pulsed electron nuclear double resonance (ENDOR), and electron spin echo envelope modulation (ESEEM) [2–4]. This dramatically extended EPR's capabilities in studies of the hyperfine interactions unresolved in the EPR spectra of solids. An important step in the development of pulsed EPR spectroscopy was initiated by a publication from Höfer et al. [5] that appeared in 1986. This article proposed a 2D experiment based on the four-pulsed ESEEM sequence, called HYperfine Sublevel CORrElation (HYSCORE) spectroscopy. HYSCORE spreads the nuclear frequencies across two dimensions, giving an unparalleled level of resolution into the hyperfine and quadrupole interactions. With the subsequent appearance of commercial-pulsed EPR spectrometers E380 and ELEXSYS E580 on the market produced and distributed by Bruker BioSpin (https://www.bruker.com/products/mr/epr.html), HYSCORE quickly became recognized as an important tool for structural characterizations of paramagnetic centers. For the last 25 years, researchers have employed HYSCORE to resolve individual contributions in multinuclear spectra and to characterize the hyperfine and quadrupole parameters.

The theoretical background developed for $I = ½$ nuclei provides simple methods for the analysis of experimental HYSCORE spectra for oriented structures as well as for orientation-disordered systems. However, the growing collection of a significant set of experimental ^{15}N HYSCORE spectra of semiquinones in protein samples that were the major topic of our research over the years has caused us to notice artifacts in the spectral lineshape or line intensities not described by the currently available theoretical models. To remedy this, we were able to explain all of the observed artificial phenomena in ^{15}N spectra of semiquinones by considering a single mechanism—strain of the hyperfine interaction.

In this review article, we give an introduction to the HYSCORE experiment and its theoretical background for spectra of $I = 1/2$ nuclei, followed by a description of the observed lineshape distortions and an explanation of how the influence of hyperfine strain on these spectra reproduces these distortions. In the final part of the article, we discuss similar line distortions found in previously published spectra from other $I = 1/2$ nuclei that suggests a broad impact of hyperfine strain on 2D spectra.

2 HYSCORE Experiment

An advantage of pulsed EPR is that the relaxation properties of the paramagnetic center, and its interactions with surrounding electron and nuclear spins, can be explored using a variety of pulse sequences. These can be configured so as to be suitable for either one-dimensional or multi-dimensional experiments. For instance, the application of 1D ESEEM spectroscopy for structural studies of the paramagnetic centers traditionally employs two-pulse ($\pi/2$–τ–π–τ–echo) and three-pulse ($\pi/2$–τ–$\pi/2$–T–$\pi/2$–τ–echo) sequences [3, 4].

The two sequences introduced above give significantly different echo decay relaxation times, which substantially affects the resolution of the ESEEM spectra. The relaxation time of the two-pulse echo is governed by the phase memory time T_m. This time does not usually exceed several microseconds in solids at low temperatures. The decay of the three-pulse echoes is controlled by the longitudinal relaxation time T_1, which is at least ~ 10- to 100-fold longer than T_m and this allows one to collect a more prolonged acquisition interval for the echo envelope [2–4].

An important problem in 1D spectroscopy is the increasing complexity of the spectra when even a small number of magnetically non-equivalent nuclei interact with an electron spin, because the congestion of lines and their overlap significantly reduces the spectral resolution and seriously complicates the interpretation. A promising way to overcome these difficulties is through multi-dimensional techniques. The simplest implementation of a 2D ESEEM experiment employed a three-pulse sequence, where a set of stimulated ESEEM patterns was recorded as a function of time $\tau + T$ at different times τ [6]. However, this experiment resulted in different linewidths along the τ and the $\tau + T$ axes controlled by T_m and T_1, respectively.

An advanced version of the 2D experiment named HYSCORE (Hyperfine Sublevel CORrElation) based on the four-pulse ($\pi/2$–τ–$\pi/2$–t_1–π–t_2–$\pi/2$–echo) sequence was proposed by Höfer et al. [5]. Within a few years, the invention of this experiment and the appearance of Bruker Biospin's pulsed EPR instruments led to the progressive surge of 2D ESEEM applications in the structural studies of paramagnetic species in chemical and biological systems. HYSCORE is nowadays the standard 2D technique used in pulsed EPR applications, because its uniform spectral resolution across both dimensions and reasonable sensitivity make it an appealing experiment to be performed for samples containing a limited concentration of paramagnetic species.

2D ESEEM spectra discussed in this article were obtained using HYSCORE. In this experiment, the intensity of the stimulated echo inverted by the π pulse is measured as a function of times t_1 and t_2 at constant time τ. Such a set of echo envelopes give, after complex Fourier transformation (FT), a 2D spectrum with equal resolution in both dimensions determined by T_1.

The essential advantage of the HYSCORE experiment is the ability to create, in 2D spectra, off-diagonal cross-peaks correlating nuclear frequencies from the $m_s = 1/2$ and $-1/2$ manifolds belonging to the same nucleus [5, 7]. These features significantly simplify the interpretation of the multinuclear experimental spectra and the determination of the hyperfine (especially for nuclear $I = 1/2$ spins) and nuclear quadrupole tensors.

3 Theoretical Background for HYSCORE Spectra of $I = 1/2$

HYSCORE spectra are sensitive to the relative signs of the correlated frequencies and are usually represented by two quadrants, (++) and (+−), of the 2D Fourier transform [7]. A nucleus with $I = 1/2$ has only two hyperfine frequencies, ν_α and ν_β, corresponding to the two states $m_s = \pm 1/2$ of the electron spin in the applied magnetic field and may produce a pair of cross-peaks (ν_α, ν_β) and (ν_β, ν_α) in the (++) quadrant, and another pair ($-\nu_\alpha$, ν_β) and (ν_α, $-\nu_\beta$) in the (+−) quadrant (Fig. 1). The ($|\nu_\alpha|$, $|\nu_\beta|$) cross-peak intensity is generally distributed between both quadrants of the HYSCORE spectrum for oriented systems [8, 9].

In a powder-type 2D spectrum, ν_α and ν_β vary in a correlated manner over the entire interval between $\nu_{\alpha(\beta)\perp} = |\nu_I \pm (a\text{–}T)/2|$ and $\nu_{\alpha(\beta)\|} = |\nu_I \pm (a + 2T)/2|$ forming a pair of cross-ridges described by the following equation [10]:

$$\left|\upsilon_{\alpha(\beta)}\right| = \left(Q_{\alpha(\beta)}\upsilon^2_{\beta(\alpha)} + G_{\alpha(\beta)}\right)^{1/2}, \tag{1}$$

where $Q_{\alpha(\beta)} = \frac{T+2a-(+)4\upsilon_I}{T+2a+(-)4\upsilon_I}$ $\quad G_{\alpha(\beta)} = \frac{+(-)2\upsilon_I\left(4\upsilon_I^2-a^2+2T^2-aT\right)}{T+2a+(-)4\upsilon_I}$,

$Q_{\alpha(\beta)}$ and $G_{\alpha(\beta)}$ are coefficients that are functions of a, T, and the Zeeman frequency ν_I. The ridge or contour lineshape forms a smooth arc extending between the points ($\nu_{\alpha(\beta)\perp}$, $\nu_{\beta(\alpha)\perp}$) and ($\nu_{\alpha(\beta)\|}$, $\nu_{\beta(\alpha)\|}$) located on the $|\nu_\alpha \pm \nu_\beta| = 2\nu_I$ lines and is confined to the area within these lines.

For characterization of the hyperfine interaction strength, one can introduce the parameter $\delta = |2a + T| - 4\nu_I$. Figure 2 shows the location of cross-ridges calculated using Eq. [1] for two hyperfine tensors with $a = 0.1$ MHz and $T = 0.8$ MHz, $\delta = -3$ MHz (A), and $a = 4$ MHz and $T = 1.8$ MHz, $\delta = 5.8$ MHz (B) (for Zeeman frequency $\nu_I = 1$ MHz) illustrating these considerations. On the other hand, analysis

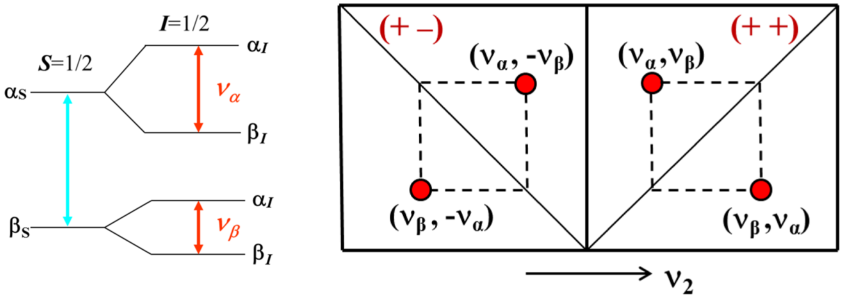

Fig. 1 (Left) Energy levels and electron and nuclear transitions in an $S = 1/2$ and $I = 1/2$ spin system. (right) Cross-peak correlation of nuclear frequencies from a spin $I = 1/2$ in the (++) and (+−) quadrants of the HYSCORE spectrum

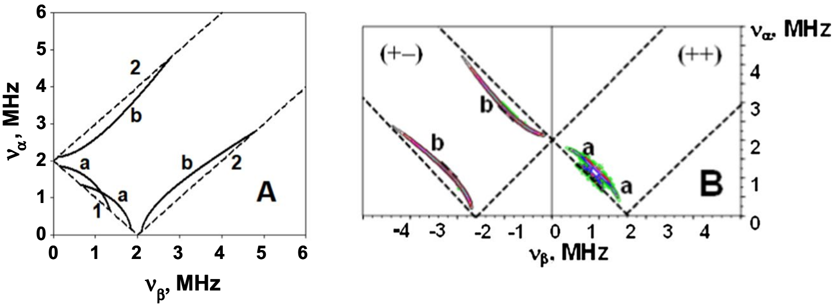

Fig. 2 **A** Location of cross-ridges in 2D spectra calculated using Eq. [1] for two nuclei with hyperfine tensors (left) $a = 0.1$ MHz, $T = 0.8$ MHz (weak hyperfine interaction case $\delta = |T + 2a| - 4\nu_I < 0$) and **b** $a = 4$ MHz and $T = 1.8$ MHz (strong hyperfine interaction case $\delta = |T + 2a| - 4\nu_I > 0$) (Zeeman frequency $\nu_I = 1$ MHz); **B** Location of cross-ridges from the same nuclei in the spectrum calculated using theoretical expressions for HYSCORE intensity. The dashed lines **1** and **2** are defined by $|\nu_\alpha + \nu_\beta| = 2\nu_I$ and $|\nu_\alpha - \nu_\beta| = 2\nu_I$, respectively. Adapted from Dikanov [12] with permission from The Royal Society of Chemistry

of theoretical expressions for HYSCORE intensity from $I = 1/2$ and spectral simulations show that only cross-ridges of weakly coupled nuclei with $\delta < 0$ and $Q_{\alpha(\beta)} < 0$ are present in the (++) quadrant of orientation-disordered spectra. In contrast, the cross-ridges from strongly coupled nuclei with $\delta > 0$ and $Q_{\alpha(\beta)} > 0$ are located in the (+−) quadrant. This effect was explained by the phase interference between coherences from different orientations of the paramagnetic species [11].

One can also note that the given description of contour lineshapes can be extended to an analysis of powder 2D spectra from several nuclei of $I = 1/2$ spin. The presentation of the cross-ridge equation [1] in the form

$$\nu^2_{\alpha(\beta)} = Q_{\alpha(\beta)}\, \nu^2_{\beta(\alpha)} + G_{\alpha(\beta)}, \tag{2}$$

indicates that the cross-ridges transform into straight line segments in $(\nu_1)^2$ vs $(\nu_2)^2$ coordinates. The slope $Q_{\alpha(\beta)}$ and intercept $G_{\alpha(\beta)}$ of each segment determine the isotropic (a) and anisotropic (T) parts of the hyperfine tensor [10].

4 ^{15}N HYSCORE Spectra from Hydrogen-Bonded Semiquinones

4.1 Experimental Results

In the last 15 years, collaborative work between Dr. Dikanov's pulsed EPR group and the biochemical laboratories of Drs. Crofts, Gennis and Wraight at the University of Illinois at Urbana-Champaign was specifically focused on the semiquinone radicals formed during electron transport in bacterial respiratory and photosynthetic electron-transfer chains [12]. Quinones play a unique role in electron transport chains, acting as (i) converters between 1 and $2e^-$ redox chemistry, and (ii) as diffusing oxidants and reductants that shuttle redox equivalents and protons between membrane enzymes (Figure S1). Electron and proton transfer reactions take place at quinone binding sites (Q-sites) located within protein structures. The identification of Q-sites has relied largely on X-ray crystallography. However, limited resolution and ambiguities in the redox states of the quinones in available structures do not provide a full description of the specific interactions with the protein environment for Q-sites in the different redox states Q/SQ/QH_2.

Pulsed EPR in conjunction with isotopic labeling ($^1H/^2H$, $^{14}N/^{15}N$, ^{13}C) was applied to investigate the following characteristics of semiquinones (SQ) in the Q-sites: (i) the environment including the number of H-bonds and corresponding donors, (ii) the conformation of substituents, and (iii) the electronic structure defined by a distribution of unpaired spin density over the ring and substituents, and protein residues. Uniform or selective ^{15}N (nuclear spin $I = 1/2$) protein labeling has been widely used in these studies for characterization of the H-bond nitrogen donors, because ^{14}N (nuclear spin $I = 1$) spectra do not reveal all of the nitrogens interacting with the SQ, and ^{15}N spectra simplify an evaluation of the hyperfine tensors. Furthermore, selective ^{15}N labeling allows one to directly identify nitrogens of interest.

Pulsed EPR characterization of the SQ in Q-sites was performed for the Q_A and Q_B-sites in the bacterial reaction center, the quinone-reducing Q_i-site of the *bc*$_1$ complex from *Rhodobacter sphaeroides*, and the Q-sites in two proton-pumping oxygen reductases *E. coli* cytochrome (cyt) *bo*$_3$ ubiquinol oxidase and *Bacillus subtilis* cyt *aa*$_3$-600 menaquinol oxidase (Figure S1) [12]. The two oxidases are close homologues with an almost identical set of four residues for quinone binding: R71(R70), D75(D74), H98(H94), Q101(E97) in cyt *bo*$_3$ (cyt *aa*$_3$-600). In addition, a pulsed EPR investigation of the nitrogen H-bond donors in comparison with the wild-type proteins has been done for mutant D75H of cyt *bo*$_3$ [13] and R70H of cyt *aa*$_3$-600 [14], and cyt *bo*$_3$ with menaquinone incorporated instead of native ubiquinone [15]. Similar pulsed EPR studies of H-bond nitrogen donors were also performed for a SQ in the Q_D site in *E. coli* nitrate reductase A by Dr. Grimaldi in collaboration with Dr. Prisner's laboratory [16, 17].

Among the indicated sites, Q_A, Q_B, Q_i and Q in cyt *bo*$_3$ function using ubiquinone, whereas the Q-site in cyt *aa*$_3$-600 and Q_D employ menaquinone (Fig. 3, Table 1). A more complete overview of the structure and function of protein systems where the Q-sites have been studied by 2D ESEEM is given in [12].

The pulsed EPR results defining the interaction between ^{15}N nitrogen H-bond donors and ubisemiquinone (USQ) or menasemiquinone (MSQ) in the ten proteins indicated above are collected in Table 1. According to these data, hyperfine tensors for ^{15}Ns involved in H-bonds with the SQ intermediates in different

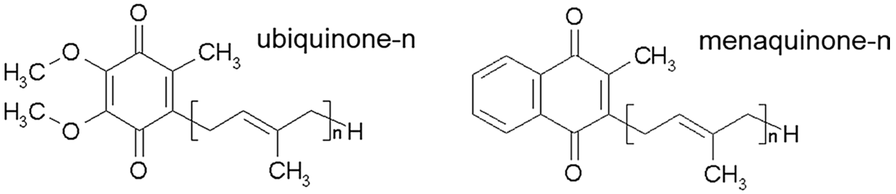

Fig. 3 Structure of ubiquinone-*n* and menaquinone-*n*

Table 1 Hyperfine couplings and corresponding parameters $2a+T$ and δ for ^{15}N nitrogen donors H-bonded with intermediate semiquinones in different proteins

Q-site and protein	Quinone	Nitrogen donor[g]	a, MHz	T, MHz	$2a+T$, MHz	δ,[a] MHz	Refs.
Q cyt bo_3	UQ_8^b	N_ε-Arg71 N_ε-His98	2.4 0.3	0.44[h] ~0.35	5.2	−0.8	[13]
Q D75H cyt bo_3	UQ_8	N_ε-His75 N_ε-His98 N_ε-Arg71	3.5 0.8 0.6	0.45[h] ~0.35 ~0.45	7.4	1.4	[13]
Q cyt aa_3-600	MQ_7^c	N_ε-Arg70	~1–1.3				[18]
Q R70H cyt aa_3-600	MQ_7	N_ε-His70	2.8	0.4	6.0	~0	[14]
Q cyt bo_3	MQ_4	N_ε-Arg71	~1.4 ~1.0 ~0.6				[15]
Q_A RC[d]	UQ_{10}	N_δ His-M219 N_p Ala-M260	3.2 3.6		6.8 7.6	0.8 1.6	[19]
Q_B RC	UQ_{10}	N_δ His-L190 N_p Gly-L225	1.9 0.6	0.49 0.2	4.3	−1.7	[20]
Q_{LM} RC LM dimer	UQ_{10}	N_δ His-L190	~2.3				[21]
Q_i cyt bc_1^e	UQ_{10}	N_ε-His217	~1.1	~0.2			[22]
Q_D NarGHI[f]	MQ_8	N_δ His-66	~1.0	0.3	2.3	−3.7	[17]

[a] $\delta = |2a+T| - 4\nu_{15N}$ for $\nu_{15N} = 1.5$ MHz corresponding to the X-band experiment with external magnetic field ~ 350 mT

[b] UQ_n, ubiquinone-n

[c] MQ_n, menaquinone-n

[d] RC, bacterial reaction center from *Rhodobacter sphaeroides*

[e] cyt bc_1, ubiquinol: cyt *c* oxidoreductase from *Rb. sphaeroides*

[f] NarGHI, *E. coli* nitrate reductase A

[g] Designations of the nitrogens in *L*-Arg and *L*-His are shown in Figure S13; N_p is the nitrogen from the peptide backbone of the corresponding amino acid

[h] Obtained from averaging the two smaller principal components of the anisotropic hyperfine tensor

proteins demonstrate about a 12-fold variation in the isotropic coupling a, i.e. from 0.3 to 3.6 MHz. In contrast, anisotropic components possess a stable value of $T_{15N} \sim 0.4 \pm 0.1$ MHz determined by the dipole–dipole interaction between the nitrogen and unpaired spin density localized on the p_z orbital of the nearest carbonyl oxygen and on the p orbitals of the nitrogen [23].

The variation in hyperfine coupling parameters collected in Table 1 is supported by spectral simulations of ^{15}N HYSCORE spectra (Figure S2) with the anisotropic component of the axial hyperfine tensor $T = 0.4$ MHz, isotropic coupling a between 1.4 and 4.2 MHz, and Zeeman frequency $\nu_{15N} = 1.5$ MHz (magnetic field is ~ 350 mT) [24]. This range of isotropic coupling constants corresponds to $|2a+T|$ changing in the interval from 3.2 to 8.8 MHz, and δ from − 2.8 to 2.8 MHz. ^{15}N cross-features are located only in the (++) quadrant for $-2.8 < \delta < -0.2$ MHz and only in the (+−) quadrant for $0.2 < \delta < 2.8$ MHz. They appear in both quadrants simultaneously or have comparable intensity in the very narrow interval $\delta = \pm 0.2$ MHz. The cross-ridges in these cases are parallel to one of the axes or deviate very slightly from this direction.

4.2 HYSCORE Spectrum from $I = 1/2$ Nucleus with $\delta = 0$

The condition $\delta = 0$ or $|2a + T| = 4\nu_I$ defines $\nu_{\beta(\alpha)\perp} = -\nu_{\beta(\alpha)\|} = \pm(3T/4)$, where all orientations of the paramagnetic center contribute to the same frequency $|3T/4|$, resulting in a singularity for the nuclear transition in one manifold of the 1D spectrum. In 2D spectra, the theoretically predicted lineshape becomes a straight-line segment parallel to the $\nu_{\alpha(\beta)}$ axis in the interval from $\nu_{\alpha(\beta)\perp} = |a - T/4|$ to $\nu_{\alpha(\beta)\|} = |a + 5T/4|$ at $\nu_{\beta(\alpha)} = |3T/4|$ confined within the lines $|\nu_\alpha + \nu_\beta| = 2\nu_I$ (Figure S2).

The X-band ^{13}C HYSCORE spectrum of USQ$_A$ in the photosynthetic RC from *Rb. sphaeroides* reconstituted with ubiquinone ^{13}C-labeled at the quinone ring and isoprenoid tail carbons provides an ideal experimental example of a spectrum with $\delta = 0$ (Fig. 4). It exhibits a unique spectral pattern of four straight ridges of similar intensity in both the (++) and (+−) quadrants, all with a common frequency in one dimension of $|3T/4| = 1.8$ MHz, allowing for an immediate calculation of the anisotropic component $T = 2.4$ MHz for the hyperfine tensor. The constraint $|2a + T| = 4\nu_{13C}$ is expected to hold in this case, where the isotropic constant is determined to be either $a = -8.6$ or 6.2 MHz [25].

4.3 Influence of "*a*-strain" on the Spectrum with $\delta = 0$

Among the proteins collected in Table 1, the X-band ^{14,15}N HYSCORE spectra of the MSQ in the R70H cyt aa_3-600 mutant indicate the presence of one nitrogen from His70 with its hyperfine tensor satisfying the relationship $\delta \approx 0$. The cross-ridges of this nitrogen in the ^{15}N spectrum consist of a straight section parallel to the ν_1 or ν_2 axis to good accuracy as well as an additional extension along the dashed line described by $\nu_1 + \nu_2 = 2\nu_{15N}$ (Fig. 5).

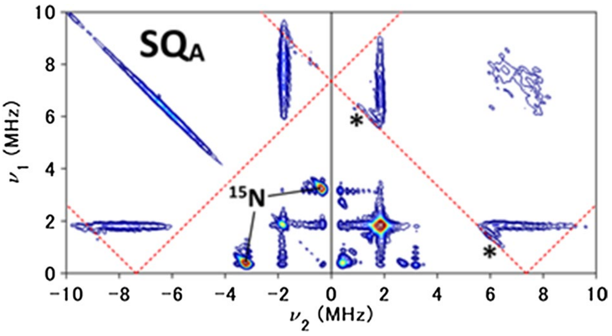

Fig. 4 X-band ^{13}C HYSCORE spectrum for USQ$_A$ in contour mode recorded with the time between the first and second pulses as $\tau = 136$ ns. The dashed lines are defined by $|\nu_1 \pm \nu_2| = 2\nu_{13C}$. Experimental parameters: microwave frequency = 9.631 GHz, magnetic field = 343.4 mT, temperature = 90 K. Adapted with permission from Taguchi et al. [25]. Copyright 2017 American Chemical Society

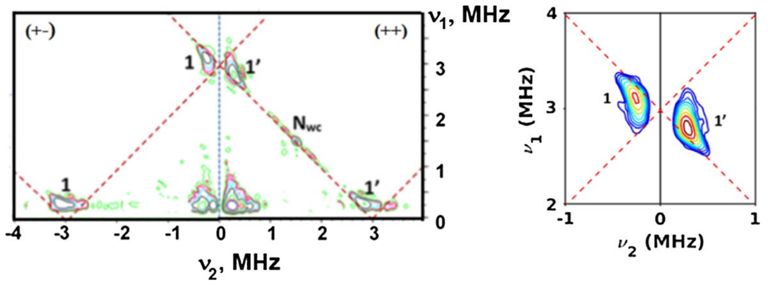

Fig. 5 Contour (left) presentation of the ^{15}N HYSCORE spectrum of MSQ in ^{15}N uniformly labeled R70H cyt aa_3-600 and (right) zoomed in view of cross-ridges **1** and **1′**. The dashed straight line segments are defined by $|\nu_1 \pm \nu_2| = 2\nu_{15N}$. Experimental parameters: magnetic field 343.25 mT, time between first and second pulses $\tau = 136$ ns, microwave frequency 9.625 GHz, temperature 60 K. Adapted with permission from Yi et al. [14]. Copyright 2015 American Chemical Society

This "boomerang-type" curvature is inconsistent with the straight segments theoretically predicted for a hyperfine tensor with $\delta = 0$ (Figure S2) as experimentally observed in the ^{13}C spectrum of the USQ$_A$ (Fig. 4).

To understand this apparent discrepancy between experiment and theory, we questioned whether or not the assumption of a static molecular structure used in the theoretical model was valid. The paramagnetic samples in single crystals and frozen solutions usually come with a distribution of structural conformations. In EPR spectroscopy, it leads to a distribution of the parameters characterizing the *g*- and hyperfine tensors. This phenomenon is more commonly referred to as "*g*- or *A*-strain", respectively. Evidence for such distributions was reported and discussed for many different samples including proteins and metallocomplexes in frozen solutions [26–28].

Based on this knowledge, it was logical to suggest that some kind of hyperfine coupling strain is responsible for the line distortion in the ^{15}N HYSCORE spectrum of MSQ in R70H of cyt aa_3-600. The experimentally observed lineshape distortions in this case were reproduced under the assumption of ^{15}N isotropic hyperfine coupling "*a*-strain". Using a Gaussian distribution for modeling *a*-strain

$$f(\Delta a) = \left[\sigma(2\pi)^{1/2}\right]^{-1}\exp\left[-(\Delta a)^2/2\sigma^2\right], \tag{3}$$

the best agreement was obtained with a standard deviation $\sigma_{15N} = 0.35$ MHz, i.e. slightly larger than 10% of the isotropic coupling (Figure S3) [14].

The isotropic coupling $a \sim 3$ MHz corresponds to a 2*s* spin density population ~ 1.4×10^{-3}, based on the unit spin ^{15}N atomic hyperfine constant $a = 2156.4$ MHz (Table 2), and variations of the spin density ~ 10^{-4} are responsible for the observed changes in the spectral lineshape. The anisotropic coupling depends on the two contributions mentioned above and it is not clear how to correlate variations of each of them with the variations of the isotropic coupling in the case of H-bonded SQs. The anisotropic coupling originating from the unit spin occupying the *p* orbital of ^{15}N is about 15 times smaller than the isotropic

Table 2 Atomic magnetic hyperfine constants

	^{1}H	^{13}C	^{15}N^{b}	^{19}F	^{29}Si	^{31}P	^{57}Fe	Refs.
a, MHz	1422.7^{a}	3333	2156	47,934	−3995	10,201	747.2	[29]
		3777	2535	52,870	−4594	13,306		[30]
T,^{c} MHz		234.7	178.1	4079	−252.3	791.7	97.75	[29]
		268.5	194.3	4400	−285.5	917.0		[30]

[a] Experimental

[b] Recalculated from the values reported for ^{14}N [29, 30], using multiplication coefficient 1.4

[c] Maximum component of the anisotropic hyperfine tensor can be estimated by multiplying values of T in the table with the angular factor 4/5 for p orbitals and −4/7 for d orbitals

constant. This ratio between the two atomic couplings is approximately fulfilled for all atoms with spin $I = 1/2$ collected in Table 2.

The total anisotropic coupling with the N$_\varepsilon$ from His70 in this sample is about seven times smaller than the isotropic constant and variations of this coupling of a similar order would be of a few hundredths of MHz only. This contribution has been ignored for this analysis. Changes in a were targeted as the potential cause of the non-ideal lineshapes, because a (but not T) is very sensitive to variations in the hydrogen bond geometry in different proteins.

4.4 *a*-Strain Features in ^{15}N HYSCORE of WT and D75H cyt *bo*$_3$

After consideration of the special case $\delta = 0$, the next natural question is what spectral characteristics indicate the presence of hyperfine strain for arbitrary values of δ. Most hyperfine couplings collected in Table 1 were initially estimated with high accuracy from a linear fit of the cross-ridges from ^{15}N HYSCORE spectra in the squared frequency (ν_1^2 vs ν_2^2) representation using Eq. [2] in its axial or rhombic form [10], and were further analyzed by numerical simulations simultaneously modeling the ^{14}N HYSCORE and/or ^{15}N ENDOR spectra. These simulations reproduce well the location and total length of the cross-features. However, in several cases, "boomerang type" distortions of the major cross-ridges and additional minor features located in the opposite quadrant of the ^{15}N HYSCORE spectra were observed. These peculiarities were not described by the spectral simulations based on a single axial or rhombic hyperfine tensor, and their appearance had remained unexplained [13].

These additional features are illustrated by the ^{15}N HYSCORE spectra of the USQ in wild-type and D75H mutant cyt *bo*$_3$ in Figure S4. The isotropic couplings reported previously for nitrogen donors N$_\varepsilon$-Arg71 (WT) and N$_\varepsilon$-His75 (D75H) are 2.4 (N$_A$) and 3.5 (N$_B$) MHz [13], and the corresponding parameters of δ are −0.8 and 1.4 MHz, respectively, [24]. The ideal theoretically predicted cross-ridge lineshapes are arcs $\mathbf{1_A}$ and $\mathbf{1_B}$ extending between two points on the $|\nu_\alpha \pm \nu_\beta| = 2\nu_{15N}$ lines as stated above (Figure S5). The cross-ridges calculated take into account HYSCORE intensities possessing similar curvatures but suppressed intensity at the edges where the magnetic field orientations close to the principal directions of the hyperfine tensor provide the major contribution (Figure S5) [11].

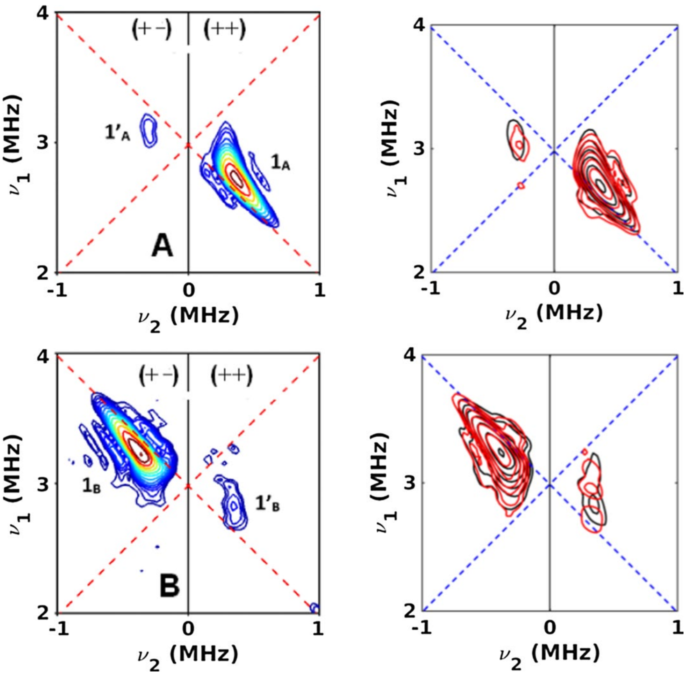

Fig. 6 Comparison of the experimental ^{15}N HYSCORE spectra for N_A and N_B (left) with the spectra calculated with a Gaussian distribution of the isotropic hyperfine coupling (right). The best fit of the spectra was obtained with $a = 2.4$ MHz, $T = 0.4$ MHz, $\sigma = 0.3$ MHz for WT cyt bo_3 (top) and $a = 3.3$ MHz, $T = 0.45$ MHz, $\sigma = 0.35$ MHz for D75H cyt bo_3 (bottom). Full spectra are shown in the Figure S4. Adapted with permission from Dikanov et al. [24]. Copyright 2018 American Chemical Society

Comparison of the experimental and calculated spectra (Figs. 6, S4, and S5) indicates that the major features $\mathbf{1_{A,B}}$ possess curvatures reversed relative to the arc shape in the calculated spectra. In addition, short cross-ridges of low intensity ($\mathbf{1'_{A,B}}$) parallel to the coordinate axes are present in opposite quadrants of both spectra.

Calculations of the spectra with a Gaussian distribution for the isotropic hyperfine couplings gives the best fit with the experimental spectra for parameters of the hyperfine tensor close to those provided above and a standard deviation similar to that observed for the MSQ in R70H cyt aa_3-600 of $\sigma = 0.35$ MHz for $\delta = 0$ (Figure S3). The close values of σ across different quinone sites likely reflect a similar mechanism of structural heterogeneity in the interaction of the SQ with the protein environment. The optimization of σ in the simulations is based more on matching the “boomerang” lineshape of the cross-ridges than the weak lineshape appearing in the opposite quadrant. On the other hand, for simulations of spectra with $\delta \sim 0$ MHz, the boomerang lineshape must be reproduced in both quadrants.

One can note that the ^{15}N HYSCORE spectra for the USQ of the Q_A site of the photosynthetic RC clearly display characteristics of a-strain not captured by our previous simulations which did not account for *a*-strain at that time [19]. However, a more complex approach including selective ^{15}N labeling is required for this site, where two H-bond N donors possessing very similar isotropic couplings $a = 3.2$ and 3.6 MHz contribute to the spectra that would interweave the individual *a*-strain features.

4.5 Calculated Influence of *a*-Strain for $\delta \neq 0$

HYSCORE simulations were performed for nitrogens N_A and N_B, where the isotropic hyperfine strain was modeled with Gaussian Eq. (3) and triangle $f(\Delta a) = (\Delta a_0)^{-1}(1 - |\Delta a/\Delta a_0|)$ distributions (Figures S6 and S7) [24]. These simulations characterize the relationship between the values of the *a*-strain width and the appearance of cross-ridge lineshape distortions. Progressive deviations of the cross-ridges from their initial shape accompanied by a change in curvature and formation of a tail parallel to the nearest $\nu_{\alpha(\beta)}$ axis take place in the interval $|\delta/4| < \Delta a_0 < |\delta/2|$. This suggests that in this interval, the condition $\delta \pm 2\Delta a \sim 0$ (depending on the sign of δ) is approached that would lead to the appearance of subsections of the cross-ridges with a heterogeneous mixture of $Q_\alpha \sim (\delta - (+)\ 2\Delta a)/8\nu_{15N}$ and $Q_\beta = 1/Q_\alpha$ (Figure S8) and would explain qualitatively the observed behavior in lineshape changes.

The condition $\delta \pm 2\Delta a = 0$ becomes satisfied at the distribution width $\Delta a_0 = |\delta|/2$. The tail in the form of a straight segment with $\nu_{1(2)} = |3T/4|$ appears in the simulated spectra at $\Delta a_0 \sim |3\delta/4|$ when part of the broadened cross-ridge possesses sufficient intensity for its observation. Simultaneously, low-intensity features parallel to the coordinate axes begin to appear in the opposite quadrant and reach an intensity maximum at $\Delta a_0 \sim |\delta|$.

5 HYSCORE Spectra from Other Nuclei with Distorted Lineshapes

5.1 General Comments

Potentially, one can expect the existence of *a*-strain effects for any $I = 1/2$ spin. Currently available HYSCORE spectra reported for $I = 1/2$ nuclei are shown in Table 3.

Table 3 Characteristics of $I = 1/2$ nuclei

Nucleus	^{1}H	^{13}C	^{15}N	^{19}F	^{29}Si	^{31}P	^{57}Fe	^{77}Se
NA %[a]	99.985	1.11	0.366	100.0	4.67	100.0	2.15	7.6
$4\nu_I$, MHz (S)[b]	20.76	5.22	2.10	19.55	4.13	8.41		3.97
$4\nu_I$, MHz (X)[b]	59.6	15.0	**6.04**[c]	56.11	**11.85**	**24.15**	1.94	11.4
$4\nu_I$, MHz (Q)[b]			20.7				**6.65**	

[a] Natural abundance

[b] Frequencies calculated for the magnetic field 122 mT (S-band), 350 mT (X-band), 1200 mT (Q-band)

[c] Bold indicates the nucleus and pulsed EPR band most likely to show evidence of hyperfine strain in HYSCORE spectra as discussed in this article

Among these, only ^{1}H, ^{31}P, and ^{19}F exist at natural abundance close to 100%. Experiments with other nuclei usually require preparation of isotopically labeled molecules or media. The spectra were collected for paramagnetic species of radicals, complexes, and clusters in frozen solutions and powder-type samples. Considering the properties of powder-type X-band 2D spectra, the strain effects are most probable to be resolved for ^{13}C and ^{31}P in addition to ^{15}N, because it requires nuclei with moderate isotropic couplings of 5–10 MHz to satisfy the condition $\delta \sim 0$ (Table 3).

Table 3 shows that by employing the multifrequency approach, one can expand the range of hyperfine couplings suitable for observing a-strain effects to lower and/or higher values. For instance, S-band spectra would allow examination of a-strain for protons with couplings ~ 8–12 MHz, and Q-band is appropriate for similar ^{15}N couplings and ^{57}Fe with couplings ~ 3–4 MHz. To support these expectations, we have examined a number of available experimental spectra reported for systems of interest. Even after consideration of a relatively limited quantity of publications we were able to find examples of HYSCORE spectra for ^{15}N, ^{31}P, ^{29}Si, and ^{57}Fe showing lineshape distortions consistent with that discussed above and indicating the possible existence of a-strain phenomenon in different systems and potentially for all $I = 1/2$ nuclei. The purpose of this search was not to give a complete review of the available spectra. The quality of many examined spectra was not sufficient for a detailed discussion of the cross-feature lineshapes. Therefore, we have focused on several examples where the spectral quality allowed us to make conclusions about the distortions of the lineshape typical of a-strain. Below, we discuss the results of our analysis in greater depth.

5.2 ^{15}N HYSCORE of Model [Fe–Fe] Hydrogenase Complex

The mixed-valence EPR active $[Fe_2(\mu\text{-}CO)(CO)_3(CN)_2\{MeSCH_2C(Me)(CH_2S)_2\}]^{1-}$ complex is structurally closely related to the redox active binuclear part of the H-cluster of the [Fe–Fe] hydrogenase in its CO-inhibited oxidized state (Figure S9) [31]. The experimental and simulated ^{15}N HYSCORE spectra of this complex are produced by two C^{15}N ligands coordinated to different irons of the Fe(I)–Fe(II) species (Fig. 7). Simulations of the experimental spectra provided two ^{15}N hyperfine tensors for strongly $a = 2.4$ MHz, $\boldsymbol{T} = [-1.1,\ 1.8,\ -0.7]$ MHz and weakly $a = 0.16$ MHz, $\boldsymbol{T} = [-0.31,\ 0.34,\ -0.02]$ MHz coupled nitrogens. The tensor of the strongly coupled ^{15}N at 342.4 mT defines $\delta = 5.7–5.9 = -0.2$ MHz for the average $T = 0.9$ MHz.

The orientation-selective simulated spectrum exhibits two straight cross-ridges in the (++) quadrant parallel to the coordinate axes to high accuracy and located within the area defined by $|\nu_\alpha \pm \nu_\beta| = 2\nu_{15N}$ (lines parallel and normal to diagonal in Fig. 7). Despite the difference in the anisotropic coupling, the simulated spectrum is in agreement with our model simulations in Figure S2 showing the appearance of cross-ridges only in the (++) quadrant (spectrum with $a = 2.7$ MHz, $T = 0.4$ MHz and $\delta = -0.2$ MHz). On the other hand, the experimental spectrum clearly exhibits visible curvature of the cross-ridges predicted by our model simulations taking into account the strain of hyperfine coupling, suggesting the existence of this

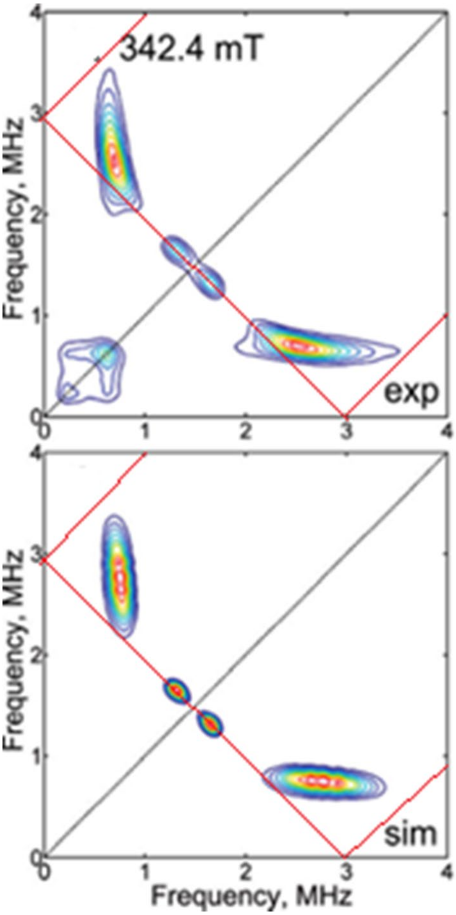

Fig. 7 X-band HYSCORE spectra (++ quadrant only is shown) of the ^{15}N-labeled model compound, measured at 342.4 mT. The simulations of the experimental spectrum were performed using the ^{15}N coupling tensors described in the text. Experimental conditions: microwave frequency, 9.7155 GHz, temperature, 20 K; shot repetition time, 7 ms; $t_{\pi/2}$, 8 ns; delay between the first and second MW pulse (τ), 280 ns; magnetic field, 342.4 mT ($g = 2.027$). Adapted with permission from Silakov et al. [31]. Copyright 2010 American Chemical Society

phenomenon in this system too. Note that an accurate analysis of the influence of hyperfine strain for this spin system would require orientation-selective simulations beyond the scope of this work. Also, the rigid structure of this complex and the larger anisotropic hyperfine coupling compared to the SQ cases may require a model that considers the influence of anisotropic hyperfine strain.

5.3 ^{57}Fe HYSCORE of [Fe–Fe] Hydrogenase

The active site of the ^{57}Fe-enriched [FeFe]-hydrogenase (i.e., the "H-cluster", Figure S9) from *Desulfovibrio desulfuricans* has been examined using advanced pulse EPR methods at X- and Q-band frequencies [32]. For the CO inhibited form (H_{ox}–CO), all six ^{57}Fe hyperfine couplings were detected indicating an apparent spin density distribution over the whole H-cluster. Four large ^{57}Fe hyperfine couplings in the range 20–40 MHz were found in the ENDOR spectra and assigned to the $[4Fe–4S]_H$ (cubane) subcluster. Two weaker ^{57}Fe hyperfine couplings < 5 MHz were identified

Fig. 8 Q-band HYSCORE spectra of [FeFe]-hydrogenase of the *D. desulfuricans* ^{57}Fe-enriched H-cluster in the H_{ox}–CO state. Experimental conditions: temperature, 20 K; length of all microwave pulses, 40 ns; delay between the first and second microwave pulse, 352 ns; microwave frequency, 33.884 GHz. Adapted with permission from Silakov et al. [32]. Copyright 2007 American Chemical Society

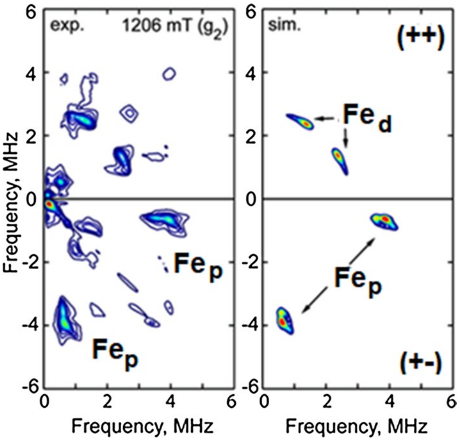

using Q-band HYSCORE spectroscopy and were assigned to the $[2Fe]_H$ subcluster (Fig. 8).

Simulations of the HYSCORE spectra of the $[2Fe]_H$ subcluster have provided ^{57}Fe hyperfine tensors $a = -4.0$ MHz, $\boldsymbol{T} = [-1.3, -0.5, 1.8]$ MHz for Fe_p, and $a = 0.8$ MHz, $\boldsymbol{T} = [1.3, 1.3, -2.5]$ MHz for Fe_d. The experimental spectra from Fe_d collected at two fields (1206 and 1174 mT) are well described by simulations with an axial hyperfine tensor and show arcing lineshapes predicted by the theoretical expression Eq. (1). Figure 8 exhibits spectra for 1206 mT as an example. In contrast, the cross-features from Fe_p simulated using rhombic tensors reproduce the locations of the experimental ones but possess completely different lineshapes. The experimental cross-ridge from Fe_p clearly shows the boomerang shape discussed above with the straight segment parallel to the nearest coordinate axis and tail extended along the $\nu_1 + \nu_2 = 2\nu_{57Fe}$ line. The authors attempted to simulate this type of lineshape for Fe_p (Fig. 8) using a rhombic anisotropic hyperfine tensor. However, the lineshape for Fe_p in the calculated spectrum is clearly different and presumably consists of three arcs with curvature opposite to that observed in the spectrum. The borders of the ideal cross-peak horn in such spectra are formed by three arc-type ridges between the pairs of three points ($\nu_{\alpha x}$, $\nu_{\beta x}$), ($\nu_{\alpha y}$, $\nu_{\beta y}$), and ($\nu_{\alpha z}$, $\nu_{\beta z}$) located on the $|\nu_1 \pm \nu_2| = 2\nu_{57Fe}$ lines [11].

The constant frequency of the straight segment in the Fe_p cross-ridge is equal to $|3T/4| = 0.65$ MHz that defines $|T| \sim 0.9$ MHz and $\delta = 0.42$ MHz. This value of T is equal to half the value of the largest component of the Fe_p tensor. It suggests that the experimental lineshape can be reproduced using an axial tensor with this T value taking into account strain of the hyperfine interaction.

Silakov et al. [33] reported Q-band ^{57}Fe HYSCORE spectra for the photoinduced state (H_{LI}) of the H-cluster, which is probably characterized by dissociation of the bridging CO ligand (Fig. 9). Simulations of the HYSCORE spectra have provided ^{57}Fe hyperfine tensors $a = 4.0$ MHz, $\boldsymbol{T} = [0.7, -0.5, -0.1]$ MHz for Fe_p, and $a = -0.2$ MHz, $\boldsymbol{T} = [3.4, -1.1, -2.4]$ MHz for Fe_d of the $[2Fe]_H$ subcluster (the original tensor $a + \boldsymbol{T}$ for Fe_d in the article is [3.4, −1.3, −2.6] MHz, but the authors

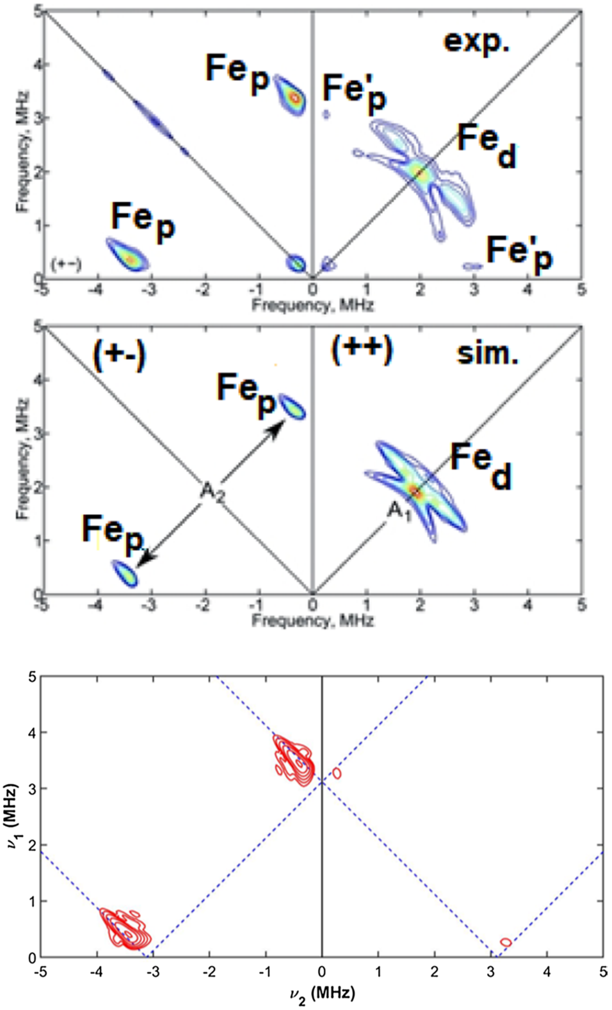

Fig. 9 Q-band HYSCORE spectrum of the ^{57}Fe-enriched H-cluster in the H_{LI} state (top), measured at $B_0 \| g_2$, together with a simulation shown below. Experimental conditions: microwave frequency 33.88 GHz, magnetic field 1134 mT; $\tau = 340$ ns; repetition time 1 ms; temperature 6 K. Adapted by permission from Copyright Clearance Center: John Wiley and Sons, Silakov et al. [33]. Copyright 2011. (bottom) Our simulation of the powder-type HYSCORE spectrum from ^{57}Fe with an axial hyperfine tensor with $a = 3.7$ MHz, $T = 0.3$ MHz, and a-strain with Gaussian standard deviation $\sigma = 0.4$ MHz. The dashed straight line segments are defined by $|\nu_1 \pm \nu_2| = 2\nu_{57\mathrm{Fe}}$

reported $a = 0.2$ MHz). In this sample, the difference between the experimental and calculated lineshapes of Fe_p indicate the presence of hyperfine strain as clearly supported by the weak straight-line segments parallel to the coordinate axes observed in the opposite (++) quadrant (one of them is resolved better than the other). The constant frequency of the straight segment defines $|3T/4| \sim 0.25$ MHz or $T \sim 0.33$ MHz, in good agreement with a half of the largest component of the anisotropic tensor.

We have attempted ^{57}Fe HYSCORE simulations to best fit the major "boomerang" peaks in the (+−) quadrant, resulting in hyperfine parameters $a = 3.7$ MHz, $T = 0.4$ MHz, and a Gaussian a-strain $\sigma = 0.4$ MHz. In addition to the major peaks, weak features in the (++) quadrant manifest as ellipses located near the border lines $|\nu_1 \pm \nu_2| = 2\nu_{57\mathrm{Fe}}$ (Fig. 9). This suggests that simultaneous fitting of a, T and σ may be necessary for an accurate estimate of the hyperfine parameters.

In summary, this review of the reported ^{15}N and ^{57}Fe spectra for the H cluster of [Fe–Fe]-hydrogenase and its model complex finds indications of hyperfine strain not only for the CN ligands, but even for the FeS(O) center itself, suggesting structural fluctuations of the entire H cluster not limited to the ligand coordination geometry.

5.4 ^{29}Si HYSCORE of Open-Shell Ti^{3+} in SiO_2–TiO_2 Mesoporous Monoliths

Silicon is a component of many surface-active materials and catalysts. The magnetic isotope ^{29}Si of silicon can be exploited as a probe in the studies of the local coordination environment of catalytically active paramagnetic species. An example of such work is reported by Morra et al. [34] devoted to CW and pulsed EPR characterization of open-shell Ti^{3+} ions generated in hybrid SiO_2–TiO_2 mesoporous monoliths. Open-shell Ti^{3+} ions are produced by reaction with triethylaluminium (TEA) vapors. The HYSCORE spectra of Ti/SiO_2 reduced with TEA show the cross-features ascribed to ^{1}H, ^{47,49}Ti, and several ^{29}Si nuclei form a naturally abundant silicon framework (Figure S10). We will focus our attention on the features assigned to two ^{29}Si with hyperfine tensors Si(1): $a = -7.4$ MHz, $\boldsymbol{T} = [1.2, 0.8, -2.10]$ MHz and Si(2): $a = -4.5$ MHz, $\boldsymbol{T} = [0.2, 0.2, -0.4]$ MHz. We note, however, that the reported simulated spectra do not reproduce the lineshape of the cross-features from Si(1) and Si(2) in the experimental spectra (Fig. 10). For Si(1), the cross-ridge is an ark with the edges oriented towards the $\nu_1 + \nu_2 = 2\nu_{29\mathrm{Si}}$ line, and the spectrum from the Si(2) is a circle of small radius instead of a straight line segment parallel to the nearest coordinate axis. One can suggest that the authors used rhombic hyperfine tensors in the simulations in an attempt to better fit the simulated lineshapes to the experimental spectra. However, cross-ridges produced by rhombic tensors consist of three arc shapes that cannot fit the boomerang-type lineshape. On the other hand, the spectrum calculated using an axial hyperfine tensor with $a = -7.4$ MHz, $T = 1.0$ MHz, and a-strain with standard deviation $\sigma = 0.8$ MHz reproduces the distorted shape of the cross-peaks Si(1) in the (+−) quadrant and the straight line segment in the (++) quadrant simultaneously in contrast to the spectrum simulated for two different nuclei with fixed hyperfine tensors. However, this result has yet to be verified by full orientation-selective spectral simulations.

5.5 ^{31}P HYSCORE Spectra

5.5.1 Oxovanadium in Bones and Model Systems

In addition to the SQs in proteins discussed above, a-strain effects can also be recognized in ^{31}P HYSCORE spectra of oxovanadium complexes with

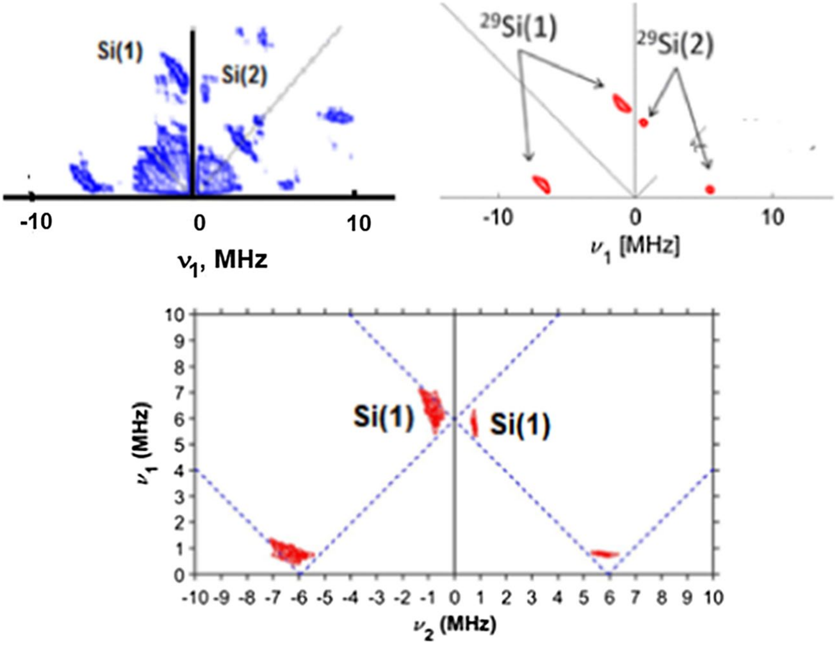

Fig. 10 (Top) Experimental (left) and simulated (right) ^{29}Si HYSCORE spectra of Ti/SiO$_2$ reduced with TEA. Experimental spectra were recorded with τ values of 192 ns and 224 ns at a magnetic field of 351.0 mT, and were added together after Fourier transformation. Adapted by permission from Copyright Clearance Center: Springer Nature, Morra et al. [34]. Copyright 2018. (bottom) Our simulation of the powder-type HYSCORE spectrum from ^{29}Si possessing an axial hyperfine tensor with $a = -7.4$ MHz, $T = 1.0$ MHz, and a-strain with standard deviation $\sigma = 0.8$ MHz. The dashed straight-line segments are defined by $|\nu_1 \pm \nu_2| = 2\nu_{29\mathrm{Si}}$

phosphates. It seems that the first example of HYSCORE spectra with cross-feature lineshapes distorted by hyperfine strain can be found in the study devoted to the coordination of the oxovanadium VO^{2+} with phosphate groups in bone from bis(ethylmaltolato)oxovanadium(IV) (BEOV) treated rats [35]. The spectra of this sample exhibit cross-ridges from three distinct ^{31}P nuclei possessing isotropic hyperfine couplings of the order ~ (14, 8, ~ 0–3) MHz and anisotropic coupling T varying between 1.1 and 2.0 MHz for all three nuclei (Figure S11). This result indicates three identifiable V–O–P (phosphate) binding modes, or several structurally distinct vanadyl–phosphate complexes in the bone mineral. With the aim of providing deeper insight into the structure of VO^{2+} coordination, the 2D-pulsed EPR work was extended to model systems including the VO^{2+}–triphosphate (TPH) complex [36] and VO^{2+} adsorbed on hydroxyapatite (HA) at different concentrations [37]. The HYSCORE spectra of VO–TPH and VO–HA both have shown the presence of three ^{31}P couplings with values similar to VO–bone samples (Table S1), suggesting a common tridentate binding motif for triphosphate moieties to the vanadyl ion. However, the relative intensities of the ^{1}H and ^{31}P cross-ridges in the HYSCORE spectra and the lineshape of

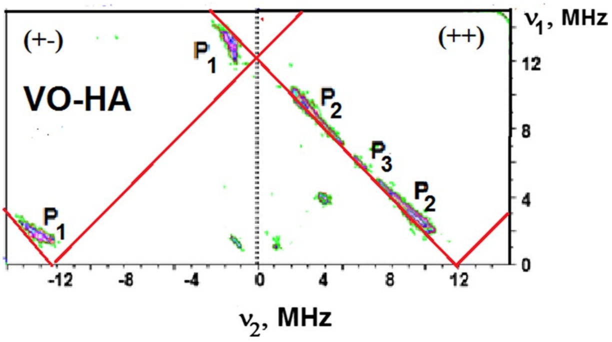

Fig. 11 Contour ^{31}P HYSCORE spectra of the VO-HA sample showing the phosphorus cross-peaks P_1–P_3. The spectra were measured at the maximum intensity of the $m_I = -1/2$ peak of the EPR spectrum. Microwave frequency = 9.710 GHz, magnetic field = 347.8 mT, $\tau = 192$ ns, T = 30 K. The straight-line segments are defined by $|\nu_1 \pm \nu_2| = 2\nu_{31P}$. Adapted by permission from Copyright Clearance Center: Taylor & Francis, Dikanov et al. [37]. Copyright 2013

the cross-feature with the smallest ^{31}P coupling indicated the formation of a 1:1 triphosphate:vanadyl VO–TPH complex in frozen solution with a varying number of equatorial phosphate ligands in VO–HA depending on the water and vanadyl content. The latter scenario can also be expected in vivo during VO^{2+} accumulation in bones. Of particular interest in these studies [35–37] for the topic of this article are the clearly distorted cross-ridges P_1 from the nucleus with the largest isotropic coupling observed in all three types of samples (Figs. 11 and S11).

In addition, one can note that very similar ^{31}P couplings were observed even earlier in HYSCORE spectra of samples where the oxovanadium cation VO^{2+} was incorporated in binding sites for Mg^{2+} in wild-type F1 ATPase (TF1) from the thermophilic bacterium *Bacillus* PS3 [38]. A ternary complex of VO^{2+} and adenosine triphosphate (ATP) with metal-depleted TF1 contains two pairs of cross-features in the HYSCORE spectra assigned to $^{31}P_\beta$ (15.5 MHz) and $^{31}P_\gamma$ (8.7 MHz) of the ATP bound with the VO^{2+} cation. Similar couplings were also obtained for an isolated VO–ATP complex. It bears mentioning, however, that spectra of both samples in [38] show evidence of a third pair of cross-peaks corresponding to weak phosphorus coupling ~ 1 MHz, similar to what is observed in VO–TPH spectra [36]. This similarity of couplings allows us to suggest that hyperfine strain may exist in these complexes too. Unfortunately, the shape of the cross-ridges similar to P_1 in the spectra from [38], recorded during the very early stage of the HYSCORE era, does not provide fully convincing support for this assumption.

5.5.2 VO^{2+} in Oxidized Bimetallic Titanium–Vanadium Microporous Catalyst

On the other hand, the HYSCORE spectra of VO^{2+} in oxidized bimetallic titanium–vanadium microporous catalyst VTiAlPO-5 exhibits cross-features from three phosphorus ^{31}P nuclei with hyperfine couplings whose relative values are close to couplings observed in VO-bone and its model complexes. The HYSCORE spectrum of the oxidized sample recorded at the powder-like position ($B_0 = 347.4$ mT)

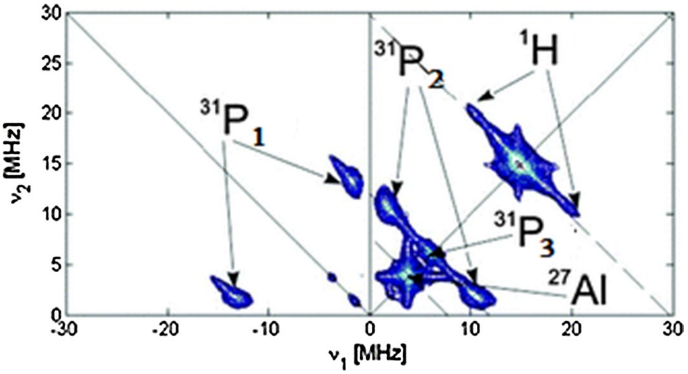

Fig. 12 HYSCORE spectrum of an oxidized VTiAlPO-5 sample at powder-like position with $B_0 = 347.4$ mT. Four spectra with τ values 96, 128, 176 and 216 ns were added together after Fourier transformation to eliminate blind spots. Adapted from Maurelli et al. [39] with permission from The Royal Society of Chemistry

is reported in Fig. 12. It contains signals from ^{31}P, ^{27}Al and ^1H nuclei. In particular, two sets of cross-peaks ($^{31}P_1$ and $^{31}P_2$) appear in the (++) quadrant approximately centered at the ^{31}P nuclear Zeeman frequency ($\nu_{31P} = 5.993$ MHz), while a third set of cross-peaks ($^{31}P_3$) appear in the (+−) quadrant separated by $2\nu_{31P}$ and positioned at approximately (− 13.8, + 1.8) and (− 1.8, + 13.8) MHz. Similar spectra were observed for the monometallic VAlPO-5 system. The characteristics of the cross-peaks $^{31}P_1$–$^{31}P_3$ led to their assignment to three phosphorus nuclei with maximum hyperfine couplings of 16, 11, and 3 MHz, respectively. In this sample, the ^{31}P cross-ridges in the (+−) quadrant also exhibit lineshapes with curvature reversed relative to an arc predicted by Eq. (1). This common observation of the lineshape distortion of the cross-ridges from ^{31}P with the largest coupling suggests strain of the isotropic coupling from the ^{31}P located in the second coordination sphere. The strain is probably caused by small deviations of the V–O bond from the coordination plane.

5.5.3 Comparison of Spectra from Different Nuclei using Normalized Parameters

In the above discussions, we have described HYSCORE spectra from different $I = 1/2$ nuclei all with similar distortions of the cross-ridges and in some cases, the appearance of weak features in the opposite quadrant resulting from hyperfine strain effects (mostly a-strain). The magnetic characteristics of these nuclei varied significantly, indicating that hyperfine strain effects can manifest under a wide variety of conditions. To allow for a quantitative comparison of spectra for different nuclei, it is necessary to normalize the parameters a, T and δ based on the corresponding Zeeman frequency of the considered nucleus (Table 4). For the normalized parameter $\delta_n = \delta/\nu_I$, the cross-features of any nucleus would be located in the (++) quadrant for $\delta_n < -0.13$ and in the (+−) quadrant for $\delta_n > 0.13$ considering the simulation shown in Figure S2. The cross-ridges parallel to one of the axes would appear

Table 4 Hyperfine parameters normalized by Zeeman frequency[a]

Sample	Nucleus	a, MHz	T, MHz	δ, MHz	δ_n
WT cyt bo_3	^{15}N	2.4 (1.6)	0.4 (0.27)	−0.8	−0.53
D75H cyt bo_3	^{15}N	3.4 (2.3)	0.45 (0.3)	1.4	0.93
Hox–CO	^{15}N	2.4 (1.6)	0.9 (0.6)	−0.2	−0.135
Hox–CO	^{57}Fe	−4.0 (2.4)	0.9 (0.54)	0.42	0.25
H_{LI}	^{57}Fe	4.0 (2.5)	0.3 (0.2)	2.0	1.27
Ti^{3+}–SiO_2	^{29}Si	−7.4 (−2.5)	−1.0 (−0.3)	3.8	1.26
VO–HA	^{31}P	~|15| (|2.5|)	2.0 (0.33)	~6	~1

[a] Normalized values of a and T are given in parentheses

in both quadrants simultaneously with comparable intensity in the narrow interval $-0.13 < \delta_n < 0.13$. The cross-ridges in these cases are parallel to one of the axes or deviate very slightly from this direction. One can see that a-strain distortions in the (++) quadrant are observed for parameters δ_n only slightly exceeding unit value and even smaller values in the (+−) quadrant. This is because a further shift of the cross-ridges from the crossing points $(0, \pm 2)$ along the straight lines would decrease the a-strain influence on the $Q_{\alpha(\beta)}$ and $1/Q_{\alpha(\beta)}$ slope.

It is interesting to note that the ^{57}Fe HYSCORE spectrum of H_{LI} and the ^{29}Si HYSCORE of the Ti^{3+}–SiO_2 sample both exhibit distortions of the cross-ridges in the (+−) quadrant and show the simultaneous appearance of weak features in the (++) quadrant. The ^{57}Fe and ^{29}Si nuclei producing these spectra possess very similar normalized hyperfine parameters recalculated from the tensors reported in the original publication (Table 4). The same can be said about D75H cyt bo_3 and VO–HA (and other VO–phosphate complexes), where their boomerang lineshapes (Figs. 6b, 11) show strong visual similarity, in agreement with their close values of normalized hyperfine parameters and δ_n, although it might be that the characteristics of the strain's distribution in VO–HA are narrower than in the case of the semiquinones. This comparison demonstrates that the described approach could be useful for a comparative analysis of spectra from different nuclei.

5.6 ^{31}P HYSCORE Spectra of a Conformationally flexible Cu(II) Complex

A different type of hyperfine strain was recently observed and analyzed in ^{31}P HYSCORE spectra of a conformationally flexible Cu(II) complex, [Cu{Ph2P(O)NP(O)Ph2-κ2O,O′}2] (complex 1) [40]. X-ray crystallography resolved two structurally distinct CuO_4 conformations of the first coordination sphere, namely a square planar and a tetrahedrally distorted one with phosphorus atoms in its second coordination sphere. Density functional theory (DFT) calculations have shown energetic equivalence of the planar and distorted forms as an intrinsic property of the Cu(II) complex. Each ligand of the complex contains two ^{31}P atoms in the second coordination sphere separated from the copper by a coordinated oxygen (Cu–O–P).

The ^{31}P HYSCORE spectra of this complex exhibit unusual inverse lineshapes of cross-features P_a (Fig. 13) that could not be reproduced by standard simulation

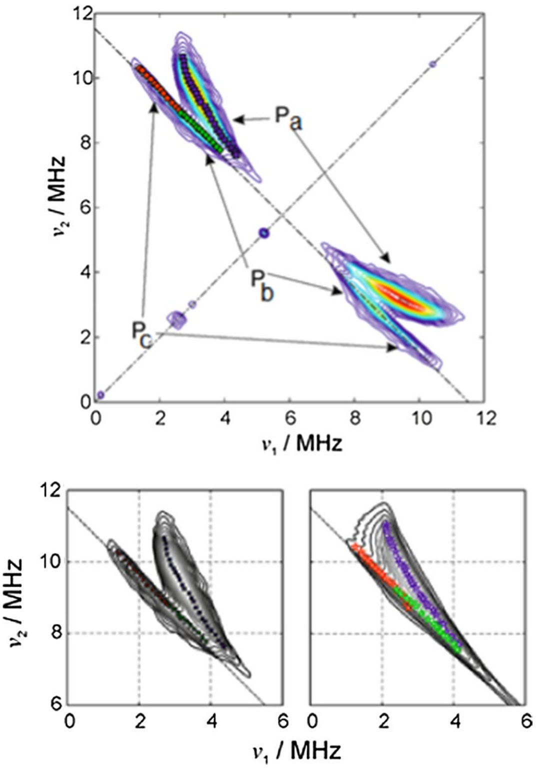

Fig. 13 (top) ^{31}P HYSCORE spectrum of complex 1 in a frozen CH_2Cl_2–toluene (1:1 v/v) solution at 30 K measured with $B_0 \parallel g_\perp$ ($B_0 = 334$ mT). The superimposed symbols denote selected points of the three cross-peaks P_a (blue squares), P_b (green diamonds), and P_c (red circles). The antidiagonal line denotes the ^{31}P Zeeman frequency, ν_{31P}. The antidiagonal dashed line is defined by the equation $|\nu_\alpha + \nu_\beta| = 2\nu_{31P}$ with $\nu_{31P} = 5.76$ MHz. (bottom) Comparison of experimental (left) and calculated (right) ^{31}P HYSCORE spectra at $B_0 \parallel g_\perp$ ($B_0 = 334$ mT). The calculated spectrum was obtained by averaging individual simulated spectra using the ^{31}P hyperfine tensors obtained with DFT and a bimodal Gaussian distribution function for isotropic couplings $a_1 = -6$ MHz, $a_2 = 6$ MHz, and $\sigma_1 = \sigma_2 = 3$ MHz. Adapted with permission from Stamos et al. [40]. Copyright 2020 American Chemical Society

procedures assuming only one set of magnetic parameters. Representation of the cross-ridges in the square frequency coordinates (Figure S12) clearly shows a strong deviation of the P_a ridge of selected points from an ideal straight line fit. Furthermore, the cross-ridge located along the antidiagonal consisting of two partially overlapping straight segments was interpreted as the superposition of two ridges P_b and P_c. The authors suggested that the observed distortion of the P_a line is produced by a significant variation of the hyperfine coupling constants resulting from structural fluctuations of the ligand near the P atoms.

Availability of the X-ray structure of the complex has allowed for a comprehensive analysis of the observed spectral features based on DFT calculations with optimized geometries for two conformations. These calculations provided the principal values of the ^{31}P hyperfine tensor for ten different snapshots with progressively increasing distortions from the planar CuO_4 geometry.

A comparison of the anisotropic hyperfine tensors obtained by DFT calculations with the T values determined from the linear regression analysis of the experimental cross-ridges shows that ridge P_a is compatible with molecular conformations close to a square planar geometry bearing positive a, whereas ridges P_b and P_c can be best ascribed to larger tetrahedral distortions and characteristic negative a values. The correlation of the strength of T with the sign of a is crucial to the simultaneous appearance of ^{31}P cross-peaks with both strong and weak anisotropy. Figure 13 demonstrates the validity of this model by comparing the experimental spectrum with the spectrum calculated as a sum of individual simulated HYSCORE contributions corresponding to different tetrahedral distortions. The spectrum shows good agreement for the peaks lying close to the anti-diagonal; however, there is a discrepancy concerning the "boomerang-shaped" ridge, P_a due to an underestimation of the T value for the simulated P_a, which can be related to the accuracy of DFT parameters which were used directly for spectral simulations and not adjusted to the experimental spectrum as in conventional HYSCORE simulations.

6 Conclusion

In this article, we presented the potential of HYSCORE spectroscopy from $I=1/2$ nuclei to resolve spectral features resulting from small structural fluctuations or different conformations not detected even in high-resolution 1D ESEEM/ENDOR spectra. It is reasonable to suggest that hyperfine strain generally influences the cross-ridge lineshape for all types of hyperfine couplings. However, clearly resolved effects from a-strain in the form of the "boomerang" lineshape and low-intensity lines in the opposite quadrant of the HYSCORE spectrum are only expected to appear when part of the strain broadened cross-ridge approaches or satisfies the condition $\delta=|2(a\pm\Delta a)+T|-4\nu_I\sim 0$. The intensity and shape of the cross-features in the opposite quadrant will depend on the strain distribution function and the Δa and δ values. In some cases, a comprehensive analysis of both the isotropic and anisotropic contributions to the hyperfine strain is required for an interpretation of the observed spectral features. The examples discussed in this article clearly show that hyperfine strain produces new spectral features in 2D pulsed EPR spectra, and ignorance of their true nature may lead to errors in spectral interpretations and resulting structural models.

Acknowledgements This work was supported by Grant DE-FG02-08ER15960 (S.A.D.) from the Chemical Sciences, Geosciences and Biosciences Division, Office of Basic Energy Sciences, Office of Sciences, U.S. Department of Energy.

This article is dedicated to the memory of Professor Yakov S. Lebedev on the occasion of his 85th anniversary. S.A.D. had the privilege to know Prof. Lebedev personally and to communicate with him during his 20 years of work at the Russian Academy of Sciences. He always received encouraging support and help from Prof. Lebedev at multiple stages of his career in the world of magnetic resonance.

References

1. E. Zavoisky, J. Phys. USSR **9**, 211 (1945)
2. J.A. Weil, J.R. Bolton, *Electron Paramagnetic Resonance. Elementary Theory and Practical Applications* (Wiley, New York, 2007)
3. A. Schweiger, G. Jeschke, *Principles of Pulse Electron Paramagnetic Resonance* (Clarendon, Oxford, 2001)
4. S.A. Dikanov, Yu.D. Tsvetkov, *Electron Spin Echo Envelope Modulation (ESEEM) Spectroscopy* (CRC Press, Boca Raton, 1992)
5. P. Höfer, A. Grupp, H. Nebenführ, M. Mehring, Chem. Phys. Lett. **132**, 2791 (1986)
6. R.P. Merks, R. de Beer, J. Phys. Chem. **83**, 3319 (1979)

7. J.J. Shane, P. Höfer, E.J. Reijerse, E. de Boer, J. Magn. Reson. **99**, 596 (1992)
8. C. Gemperle, G. Aebli, A. Schweiger, R.R. Ernst, J. Magn. Reson. **88**, 241 (1990)
9. A.M. Tyryshkin, S.A. Dikanov, D. Goldfarb, J. Magn. Reson. **105**, 271 (1993)
10. S.A. Dikanov, M.K. Bowman, J. Magn. Reson., Ser. A **116**, 125 (1995)
11. S.A. Dikanov, A.M. Tyryshkin, M.K. Bowman, J. Magn. Reson. **144**, 228 (2000)
12. S.A. Dikanov, Electr. Paramagn. Reson. **23**, 103 (2013)
13. M.T. Lin, A. Baldansuren, R. Hart, R.I. Samoilova, K.V. Narasimhulu, L.L. Yap, S.K. Choi, P.J. O'Malley, R.B. Gennis, S.A. Dikanov, Biochemistry **51**, 3827 (2012)
14. S.M. Yi, A.T. Taguchi, R.I. Samoilova, P.J. O'Malley, R.B. Gennis, S.A. Dikanov, Biochemistry **54**, 5030 (2015)
15. Z. Ding, C. Sun, S.M. Yi, R.B. Gennis, S.A. Dikanov, Biochemistry **58**, 4559 (2019)
16. R. Arias-Cartin, S. Lyubenova, P. Ceccaldi, T. Prisner, A. Magalon, B. Guigliarelli, S. Grimaldi, J. Am. Chem. Soc. **132**, 5942 (2010)
17. M. Seif Eddine, F. Biaso, R. Arias-Cartin, E. Pilet, J. Rendon, S. Lyubenova, F. Seduk, B. Guigliarelli, A. Magalon, S. Grimaldi, Chemphyschem **18**, 2704 (2017)
18. S.M. Yi, K.V. Narasimhulu, R.I. Samoilova, R.B. Gennis, S.A. Dikanov, J. Biol. Chem. **285**, 18241 (2010)
19. A.T. Taguchi, P.J. O'Malley, C.A. Wraight, S.A. Dikanov, J. Phys. Chem. B **118**, 9225 (2014)
20. A.T. Taguchi, P.J. O'Malley, C.A. Wraight, S.A. Dikanov, J. Phys. Chem. B **118**, 1501 (2014)
21. C. Sun, A.T. Taguchi, P.J. O'Malley, S.A. Dikanov, C.A. Wraight, J. Phys. Chem. Lett. **6**, 4541 (2015)
22. S.A. Dikanov, J.T. Holland, B. Endeward, D.R.J. Kolling, R.I. Samoilova, Th.F. Prisner, A.R. Crofts, J. Biol. Chem. **282**, 25831 (2007)
23. E. Martin, R.I. Samoilova, K.V. Narasimhulu, C.A. Wraight, S.A. Dikanov, J. Am. Chem. Soc. **132**, 11671 (2010)
24. S.A. Dikanov, A.T. Taguchi, J. Phys. Chem. B **122**, 5205 (2018)
25. A.T. Taguchi, P.J. O'Malley, C.A. Wraight, S.A. Dikanov, J. Phys. Chem. B **121**, 10256 (2017)
26. W.R. Hagen, *Biomolecular EPR Spectroscopy* (Taylor & Francis Group, CRC Press, Boca Raton, 2009) Chap. 9, pp. 153–168
27. W.R. Hagen, in *Advanced EPR: Applications in Biology and Biochemistry*, ed. by A.J. Hoff (Elsevier, Amsterdam, 1989), pp. 782–812
28. W. Froncisz, J.S. Hyde, J. Chem. Phys. **73**, 3123 (1980)
29. J.A.J. Fitzpatrick, F.R. Manby, C.M. Western, J. Chem. Phys. **122**, 084312 (2005)
30. J.R. Morton, K.F. Preston, J. Magn. Reson. **30**, 577 (1978)
31. A. Silakov, J.L. Shaw, E.J. Reijerse, W. Lubitz, J. Am. Chem. Soc. **132**, 17578 (2010)
32. A. Silakov, E.J. Reijerse, S.P.J. Albracht, E.C. Hatchikian, W. Lubitz, J. Am. Chem. Soc. **129**, 11447 (2007)
33. A. Silakov, E.J. Reijerse, W. Lubitz, Eur. J. Inorg. Chem. 1056 (2011)
34. E. Morra, A. Budnyk, A. Damin, M. Chiesa, Top. Catal. **61**, 1485 (2018)
35. S.A. Dikanov, B.D. Liboiron, K.H. Thompson, E. Vera, V.G. Yuen, J.H. McNeill, C. Orvig, J. Am. Chem. Soc. **121**, 11004 (1999)
36. S.A. Dikanov, B.D. Liboiron, C. Orvig, J. Am. Chem. Soc. **124**, 2969 (2002)
37. S.A. Dikanov, B.D. Liboiron, C. Orvig, Mol. Phys. **111**, 2967 (2013)
38. C. Buy, T. Matsui, S. Andrianambininstoa, C. Sigalat, G. Girault, J.-L. Zimmerman, Biochemistry **35**, 14281 (1996)
39. S. Maurelli, M. Chiesa, E. Giamello, R.M. Leithall, R. Rajab, Chem. Commun. **48**, 8700 (2012)
40. N.-A. Stamos, E. Ferentinos, M. Chrysina, C.P. Raptopoulou, V. Psycharis, Y. Sanakis, D.A. Pantazis, P. Kyritsis, G. Mitrikas, Inorg. Chem. **59**, 3666 (2020)